 doi:10.20944/preprints202207.0199.v1

Article

Effect of Ga_2O_3 Addition on the Properties of Garnet-type Ta-doped $Li_7La_3Zr_2O_{12}$ Solid Electrolyte

Yusuke Yamazaki [1], Shotaro Miyake [1], Keigo Akimoto [1], and Ryoji Inada [1,*]

[1] Department of Electrical and Electronic Information Engineering, Toyohashi University of Technology, Toyohashi Aichi 4418580, Japan; yamazaki.yusuke.td@tut.jp (Y.Y.); miyake.shotaro.of@tut.jp (S.M.); akimoto.keigo.dz@tut.jp (K.A.)

* Correspondence: inada.ryoji.qr@tut.jp; Tel.: +81-532-446723

Abstract: Garnet-type Ta-doped $Li_7La_3Zr_2O_{12}$ (LLZO) ceramic solid electrolytes with Ga_2O_3 additive were synthesized via a conventional solid-state reaction process. When the amounts of Ga_2O_3 additive were below 2 mol %, the sintered sample has a dense structure composed of grains with the averaged size of 5 to 10 μm, while 3 mol % or more Ga_2O_3 addition causes the significant increase in grain size above several 10 to 100 μm, due to the sintering with large amount of liquid Li-Ga-O phase at high temperature. The highest total (bulk + grain-boundary) ionic conductivity of 1.1 mS cm^{-1} at room temperature was obtained in the sample with 5 mol % Ga_2O_3 addition. However, in galvanostatic testing of the symmetric cell with Li metal electrodes, this sample was shorted by Li dendrite growth into solid electrolyte at current density below 0.2 mA cm^{-2}. The tolerance for Li dendrite growth is maximized in sample sintered with 2 mol % Ga_2O_3 addition, which was shorted at 0.8 mA cm^{-2} in the symmetric cell. Since the interfacial resistance between Li metal and solid electrolyte was nearly identical among the all samples, the difference in tolerance for Li dendrite growth is mainly attributed to the difference in microstructure of sintered samples depending on the amounts of Ga_2O_3.

Keywords: garnet; Li dendrite growth; solid electrolyte; solid state battery; Ga_2O_3 addition

1. Introduction

The application field of lithium (Li) ion batteries (LiBs) has been widely spreading from a power source for portable electronic devices to a large-scale one for electric vehicles (EV), plugin hybrid electric vehicles (PHEV) and stationally energy storage system for load levelling. Along with the expansion of application fields for LiBs, not only further enhancement of the energy density of batteries but also higher safety and reliability are highly required.

The replacement of a flamable organic liquid electroyte with a non-flamable solid electrolyte is recognized as a most promising way for drastical improvement of battery safety. Inorganic ceramic lithium (Li) ion conductors used as solid electrolytes are the key materials for the realization of high performance all-solid-state batteries with high safetly and reliability [1,2]. For the solid-state battery applications, the materials for the use as a solid electrolyte need to have not only good ionic conducting properties but also plasticity and excellent chemical and electrochemical stability. Although oxide-based solid electrolyte materials have rather lower ionic conductivity and poorer deformability than sulfide-based one, they have other several advantages such as their chemical stability and easiness in handling [3].

Among the various candidates, Li-stuffed garnet-type oxide with the composition of $Li_7La_3Zr_2O_{12}$ (LLZO) has been extensively investigated for the application to solid-state batteries [4–10], because of the high ionic conductivity of 10^{-4}–10^{-3} S cm^{-1} at room temperature range, good thermal stability and moderate chemical stability in air. Although the electrochemical stability of LLZO against Li metal could be affected by the dopant elements for stabilizing highly conductive cubic phase and improving ionic

Preprints (www.preprints.org) | NOT PEER-REVIEWED | Posted: 13 July 2022 doi:10.20944/preprints202207.0199.v1

conducting properties [11–13], LLZO generally shows good chemical and electrochemical stability against Li metal compared to other solid electrolyte materials.

The use of Li metal with a large gravimetric theoretical capacity (= 3,860 mAh g^{-1}) and the lowest electrode potential (= –3.045 V vs. SHE) as an anode material leads to high energy density of batteries, while the formation of a solid-solid interface between LLZO and Li metal electrode remains a challenging issue. Poor interfacial connection due to the void formation at cell assembling stage and/or during the multiple charge and discharge cycling causes non-uniform Li plating and particularly when the cell is cycled at high current densities, intergranular Li dendrite growth in polycrystalline LLZO resulting into internal short circuit failure [14–17].

Establishing the prevent technology to eliminate the possible Li dendrite growth into solid electrolyte has been positioned as a top priority issue for the realization of solid-state Li-metal batteries. To date, significant research efforts have been made to reduce the interfacial charge-transfer resistance between LLZO and Li and improve the stability against Li plating/stripping at the interface including the elimination of secondary phases by polishing or chemical etching the surface of LLZO [16,18–21], the introduction of thin film layers and thermal treatment at specific temperatures before and/or after contacting with Li [22–28], controlling the grain size and morphology of LLZO [29–37], and introduction of three-dimensional porous LLZO structure at the interface to secure Li deposition sites and reduce effective current density [38,39]. Multiscale analysis for understanding of the phenomenon occurring at the Li/LLZO interface and LLZO grain boundary areas will play a critical role to overcome this issue [40–47].

Microstrucure of LLZO is one of the main factor for the stability for Li plating and stripping, because the fracture toughness of polycristalline LLZO is strongly influenced by the density, grain size and grain-boudary structure of LLZO [30,31,35–37]. In this work, we investigated the effect of Ga_2O_3 addition on the properties for Ta-doped LLZO ($Li_{6.55}La_3Zr_{1.55}Ta_{0.45}O_{12}$). It is expected that added Ga_2O_3 will react with Li contained in Ta-doped LLZO to form Li-Ga oxides at sintering process, which form the liquid phase at 990–1000 °C [48]. Therefore, the microstructure and electrochemical properties of sintered Ta-doped LLZO may be influeced strongly by the amounts of Ga_2O_3 addition. Optimized amounts for Ga_2O_3 is discussed from the viewpoints to achieve high ionic conductivity and tolerance for Li dendrite growth.

2. Materials and Methods

2.1. Synthesis and characterization of Ta-doped LLZO with Ga_2O_3 addition

Calcined Ta-doped LLZO powder was synthesized via a conventional solid state reaction method. $LiOH \cdot H_2O$ (Kojundo Chemical Laboratory, 99%), $La(OH)_3$ (Kojundo chemical laboratory, 99.99%), ZrO_2 (Kojundo chemical laboratory, 98%) and Ta_2O_5 (Kojundo chemical laboratory, 99.9%) were weighed with the molar ratio of Li : La : Zr : Ta = 7.205 : 3 : 1.55 : 0.45 (adding 10% excess Li, considering the volatilization of Li during the sintering process). Here, the composition of Ta-doped LLZO was set to maximize the ionic conductivity based on our previous works [16,49]. Then, these starting materials were mixed and ground with ethanol for 5 hours by planetary ball-milling (Nagao System, Planet M2-3F) with zirconia balls with the diameter of 10 mm in a zirconia pot. The mixture was dried at 80 °C and then calcined at 900 °C for 6 hours in air using a Pt-5%Au alloy crucible.

1, 2, 3, 5 and 7 mol% Ga_2O_3 powder (Kojundo chemical laboratory, 99.99%) was added to Ta-doped LLZO calcined powders and ground again by planetary ball-milling for 1 hour. Then, the ball-milled powder was pelletized at 300 MPa by cold isostatic pressing. Finally, the pelletized samples were sintered at 1150°C for 15 hours in air using a Pt-5%Au alloy crucible. To suppress Li loss and the formation of secondary phases by high temperature sintering, the pellets were covered with the same mother powder. For comparison, sample without Ga_2O_3 addition was also prepared under a same condition.

Preprints (www.preprints.org) | NOT PEER-REVIEWED | Posted: 13 July 2022 doi:10.20944/preprints202207.0199.v1

Crystal phase for all sintered samples was evaluated by X-ray diffraction (XRD, RIGAKU Multiflex, Rigaku) using Cu$K\alpha$ radiation (λ = 0.15418 nm), with a measurement range of 2θ = 5–90° and a step interval of 0.002°. Microstructures for fractured cross sectional surfaces of all sintered samples were observed by a scanning electron microscope (SEM, VE-8800, Keyence). The distributions of constituent elements in Ga_2O_3 added samples were investigated by energy dispersive X-ray (EDX) analysis, using field-emission scanning electron microscope (FE-SEM, SU8000 Type II, Hitachi).

2.2. Electrochemical characterization of Ta-doped LLZO with Ga_2O_3 addition

Ionic conductivity for all sintered samples was evaluated at a temperature range from 27 to 102 °C by an electrochemical impedance spectroscopy (EIS) measurement with a frequency from 4 Hz to 2 MHz and an applied voltage amplitude of 0.01 V, using an impedance meter (IM3536, Hioki). Before the conductivity measurements, both parallel end surfaces of each sintered sample were polished and coated with Au films by sputtering as ion blocking electrodes.

Then, all samples were used for evaluating the tolerance for Li dendrite growth through the galvanostatic cycling test using a symmetric cell with Li metal electrodes. Before assembling a symmetric cell, both end surfaces of Ta-LLZO pellet were polished to remove surface contamination and the pellet thickness was controlled to 0.16 cm. Both the end surfaces of Ta-LLZO pellet were coated again with Au films (thickness = 100 nm) by sputtering. Then, the pellet was sandwiched with two Li metal foils with the diameter of 0.8 cm and thickness of 0.15 cm in a cell fixture (Hosen, KP-Solid Cell) in an argon-filled grove box followed by heating at 175 °C for 5 hours, to reduce the interfacial charge-transfer resistance (R_{int}) between Ta-LLZO and Li via alloying reaction of Li and Au [23,25,27,34,49]. It is noted that the stacking pressure of each symmetric cell was set to 4 MPa. Both introducing Au interlayer and unifying the cell stacking pressures are effective to adjust the difference in R_{int} among the samples as small as possible [34,49].

Each symmetric cell was cycled with changing the current densities from 0.05 to 1.0 mA cm^{-2} and the cell voltage response was measured using a Battery Test System (TOSCAT-3100, TOYO SYSTEM) at 25 °C, until the cell showed an evidence of Li dendrite growth and propagation into a solid electrolyte. EIS measurement was carried out at room temperature using an impedance meter before and after the cycling test to characterize the resistance of each symmetric cell.

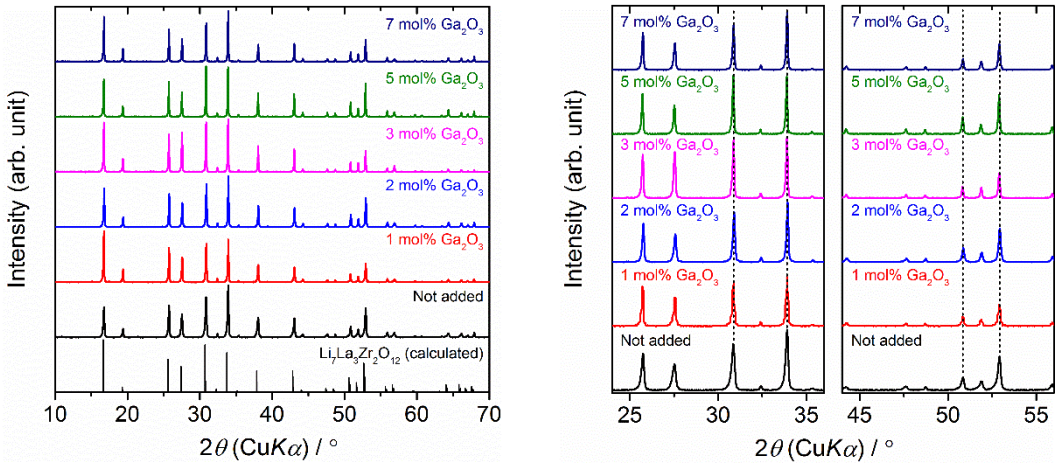

Figure 1. (a) X-ray diffraction patterns for sintered Ta-doped LLZO with or without Ga_2O_3 addition. Enlarged data at 2θ = 24–36 ° and 24–56 ° are shown in **(b)**. The calculated pattern for LLZO is also plotted in (a) as the reference.

3. Results and Discussion

Preprints (www.preprints.org) | NOT PEER-REVIEWED | Posted: 13 July 2022 doi:10.20944/preprints202207.0199.v1

3.1. Structural analysis of Ta-doped LLZO with Ga_2O_3 addition

XRD patterns for sintered Ta-doped LLZO with or without Ga_2O_3 addition are summarized in Figure 1. The calculated diffraction pattern based on the reported structural parameter for cubic LLZO is also plotted in Figure 1(a) as the reference [50]. All the peaks for sintered samples are well indexed as a cubic garnet-type structure and no other secondary phases were observed. Comparing with the calculated pattern for cubic LLZO, the peaks of sintered samples are shifted toward a higher angle 2θ. This is attributed to the reduction of lattice size of a cubic garnet phase by substitution of Zr^{4+} (72 pm) with smaller Ta^{5+} (64 pm) [16,49]. As shown in the enlarged profiles at 2θ = 24–36 ° and 24–56 ° (Figure 1(b)), peak shifts by Ga_2O_3 addition are negligibly small, so that the Ga_2O_3 addition has no notable influence on the lattice size of sintered Ta-doped LLZO.

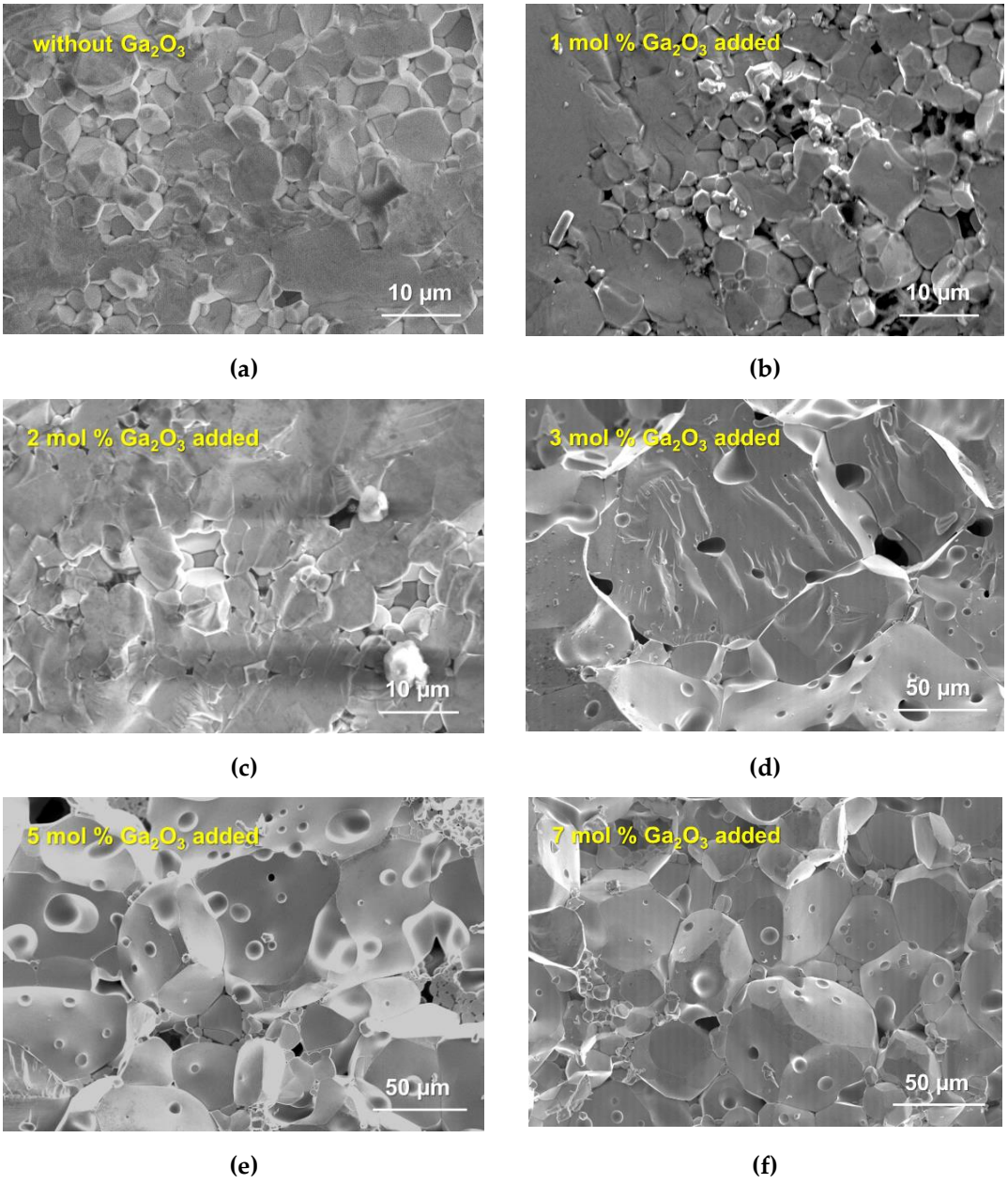

Figure 2. SEM images for fractured cross sectional surfaces of sintered Ta-doped LLZO: (a) without Ga_2O_3 addition, (b) 1 mol % Ga_2O_3 addition, (c) 2 mol % Ga_2O_3 addition, (d) 3 mol % Ga_2O_3 addition, (e) 5 mol % Ga_2O_3 addition and (f) 7 mol % Ga_2O_3 addition. Note that the scale bars in (a)–(c) are different from (d)–(f).

Figure 2 shows the SEM observation images for the fractured cross sections of sintered Ta-doped LLZO with or without Ga_2O_3 addition. Although the sintering conditions

Preprints (www.preprints.org) | NOT PEER-REVIEWED | Posted: 13 July 2022 doi:10.20944/preprints202207.0199.v1

are identical among the samples, microstructures of sintered samples are strongly influenced by Ga_2O_3 addition. When the amounts of Ga_2O_3 additive were below 2 mol %, the sintered sample has a dense structure composed of grains with the averaged size of 5–10 μm, but a few abnormally grain growth areas were confirmed. On the other hand, 3 mol % or more Ga_2O_3 addition causes the significant increase in grain size above several 10 μm and forms many micrometer-sized pores. As reported in the literature [48], Ga_2O_3 forms liquid Li-Ga-O phase at temperature of 990–1000 °C, which promote the densification of LLZO and/or LLZO grain growth via liquid phase sintering. We believe the increase in the amount of Li-Ga-O phase causes significant increase in grain sizes as observed in 3 mol% or more Ga_2O_3 added.

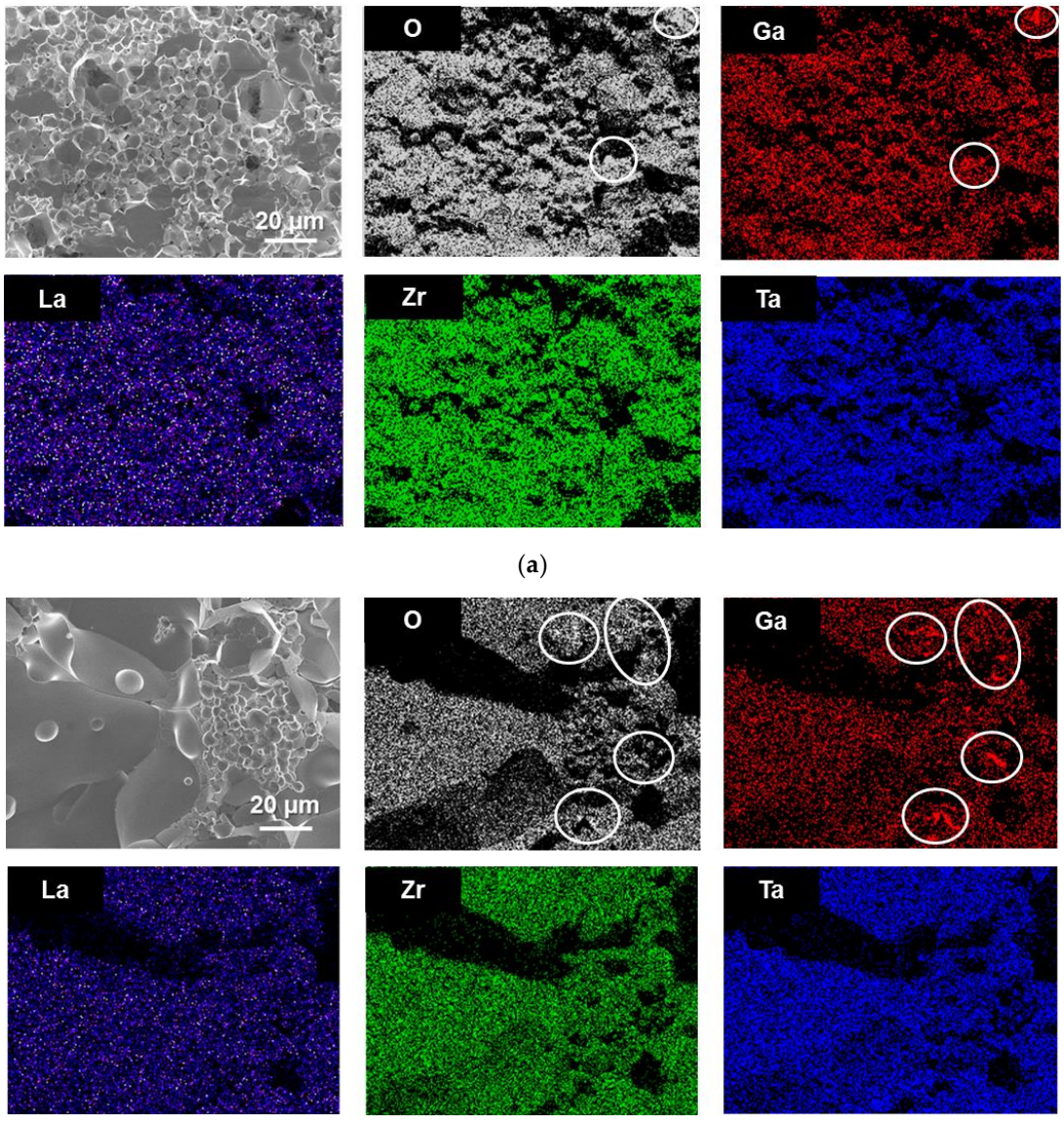

Figure 3. Constituent element (La, Zr, Ta, Ga and O) distributions on the fractured cross-sectional surfaces of Ta-doped LLZO sintered with (a) 2 mol % Ga_2O_3 and (b) 5 mol % Ga_2O_3. The segregation areas of Ga and O in each sample are marked with white-lined circles.

The distributions of constituent elements (O, La, Zr, Ta and Ga, excluding Li) on the fractured cross sectional surfaces of Ta-doped LLZO sintered with 2 mol % and 5 mol % Ga_2O_3 addition are shown in Figure 3. It is confirmed that the distribution of La, Zr and

Preprints (www.preprints.org) | NOT PEER-REVIEWED | Posted: 13 July 2022 doi:10.20944/preprints202207.0199.v1

Ta seems to be very similar in the SEM observation area for each sample. Interestingly, Ga distributes on surface of Ta-doped LLZO grains, suggesting that the small amount of Ga may be incorporated into Ta-doped LLZO. In addition, several segregation areas with Ga and O are clearly confirmed mainly at the grain boundary regions, which seems to be more remarkable in 5 mol % Ga_2O_3 added samples. Although the secondary phase by Ga_2O_3 addition were not detected in XRD measurements (Figure 1), Ga_2O_3 added sample contains the tiny amount of Ga-contained oxide.

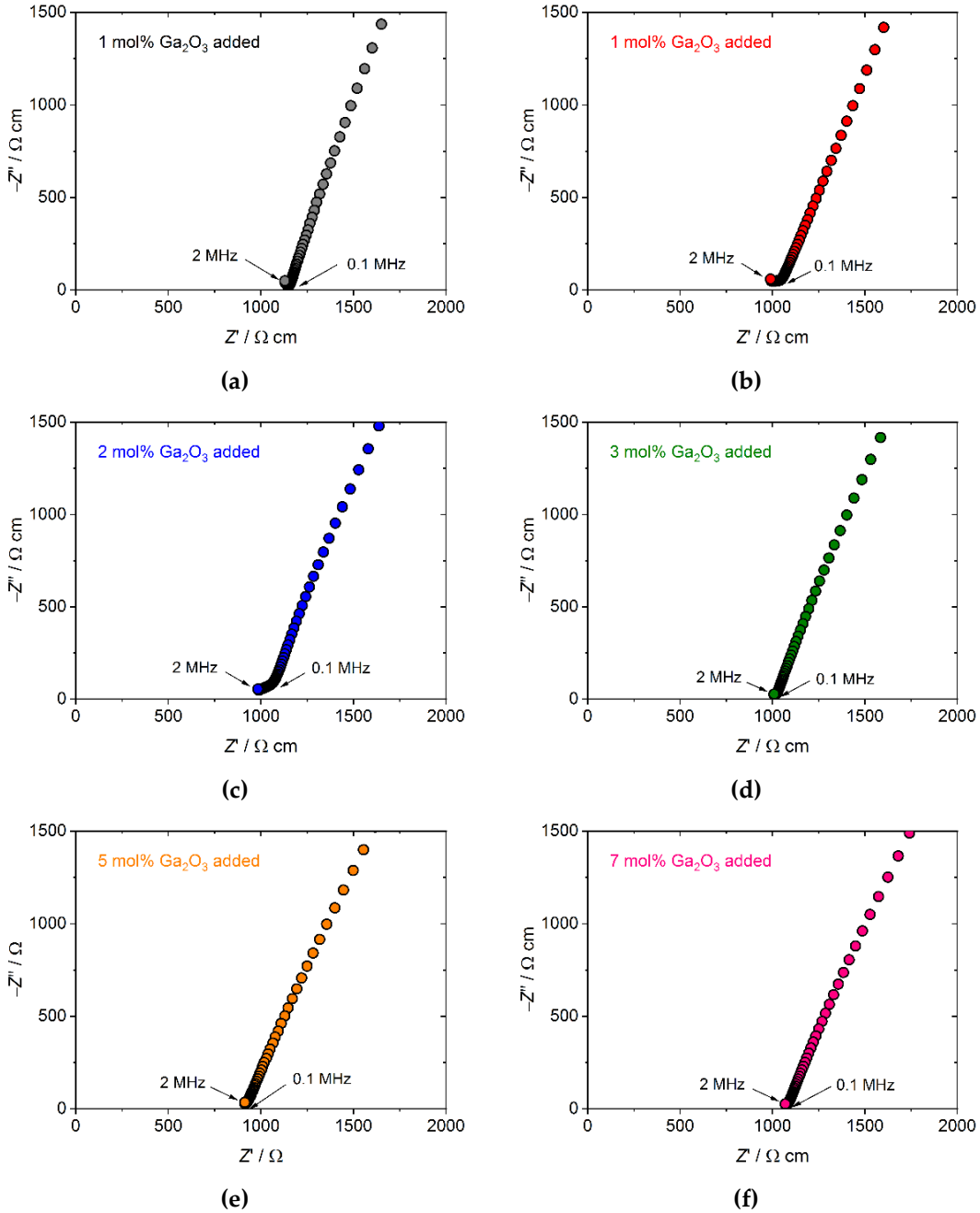

Figure 4. Nyquist plots for complex impedance $Z' + jZ''$ in Ta-doped LLZO sintered with or without Ga_2O_3 addition measured at 27 ºC: (a) without Ga_2O_3 addition, (b) 1 mol % Ga_2O_3 addition, (c) 2 mol % Ga_2O_3 addition, (d) 3 mol % Ga_2O_3 addition, (e) 5 mol % Ga_2O_3 addition and (f) 7 mol % Ga_2O_3 addition. Au ionic blocking electrodes was used for the measurement.

3.2. Ionic conductin properties of Ta-doped LLZO with Ga_2O_3 addition

Preprints (www.preprints.org) | NOT PEER-REVIEWED | Posted: 13 July 2022 doi:10.20944/preprints202207.0199.v1

Figure 4 shows the Nyquist plots for complex impedance $Z' + jZ''$ for all sintered samples with Au blocking electrodes measured at room temperature. For direct comparison of the data among the samples, real and imaginal parts of complex impedance Z' and Z'' multiplied by a factor of S/t are plotted, where S and t are the surface area and thickness of each sample. For all samples, the plot at room temperature is composed of a linear tail at frequency below 0.1 MHz and a small part of the semicircle at frequency higher than 0.1 MHz. The intersection point of the exterior straight line of the data in the linear tail and the Z' axis nearly corresponds to the total (bulk + grain-boundary) resistance R_{total} of each sample. The R_{total} values for Ga_2O_3 added samples are confirmed to be slightly smaller than the sample without Ga_2O_3 addition, suggesting that Ga_2O_3 addition has a positive effect for ionic conduction in sintered Ta-LLZO. Only for the samples sintered with 1 and 2 mol % Ga_2O_3 addition, the contribution of grain-boundary resistance is observed (Figure 4(b) and (c)), but even for them, its contribution to total resistance is small.

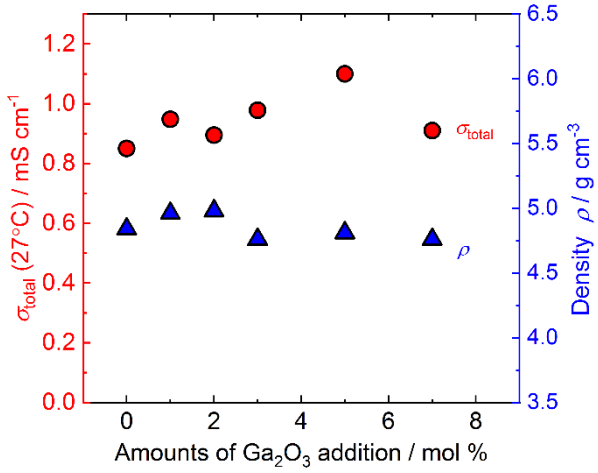

Figure 5. The density ρ and total ionic conductivity σ_{total} at room temperature of all sintered samples plotted against the amounts of Ga_2O_3 addition.

Table 1. The density ρ, total ionic conductivity σ_{total} at room temperature and activation energy E_a for Ta-doped LLZO sintered with or without Ga_2O_3 addition.

Ga_2O_3 addition / mol %	ρ / g cm^{-3}	σ_{total} at 27 °C / mS cm^{-1}	E_a / eV
None	4.84	0.85	0.38
1	4.96	0.95	0.31
2	4.98	0.90	0.36
3	4.76	0.98	0.31
5	4.81	1.1	0.33
7	4.76	0.91	0.30

Figure 5 shows the total ionic conductivity σ_{total} at room temperature for sintered Ta-doped LLZO plotted against the amounts of Ga_2O_3 addition. The density ρ of each sintered sample is also plotted in the graph, which is calculated by the mass and geometrical parameters of each sample. As can be seen, the Ga_2O_3 amount dependence of σ_{total} and ρ are slightly different. σ_{total} shows the maximum value (= 1.1 mS cm^{-1}) for the sample with 5 mol % Ga_2O_3 addition while the density becomes the highest for the sample with 2 mol % Ga_2O_3 addition. Slightly lower density of the samples sintered with 3 mol % or more Ga_2O_3 addition may be attributed to the formation of micrometer-sized pores as shown in Figure 2(d)–(f). From the temperature dependence of σ_{total} (Figure S1 in supplementary materials), the activation energy E_a for ionic conduction in each sample was estimated and summarized in Table 1 together with σ_{total} and ρ. σ_{total} at room temperature is increased slightly and E_a tends to become lower by Ga_2O_3 addition.

Preprints (www.preprints.org) | NOT PEER-REVIEWED | Posted: 13 July 2022 doi:10.20944/preprints202207.0199.v1

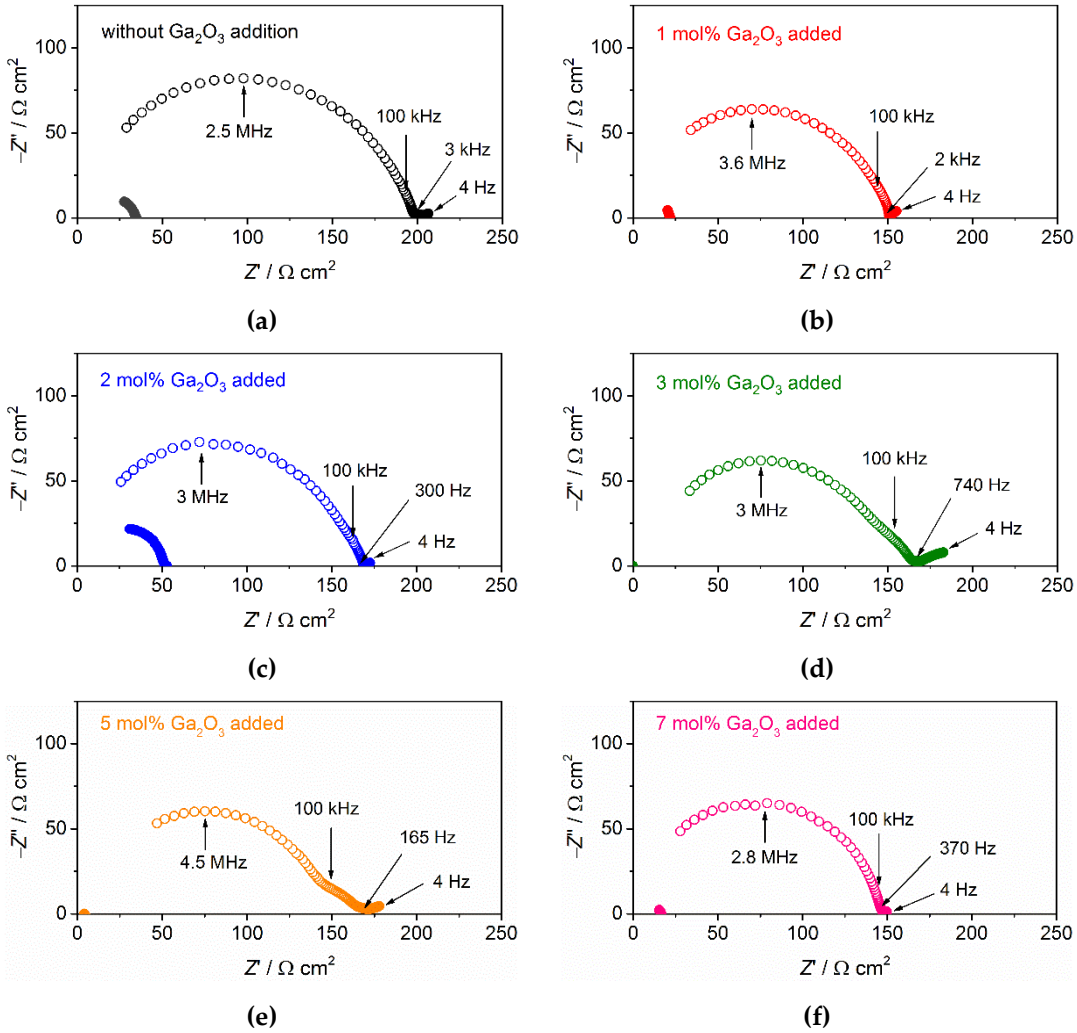

Figure 6. Nyquist plots for complex impedance $Z' + jZ''$ at 27 ºC in symmetric cells composed of Li metal electrodes and Ta-doped LLZO: (a) without Ga_2O_3 addition, (b) 1 mol % Ga_2O_3 addition, (c) 2 mol % Ga_2O_3 addition, (d) 3 mol % Ga_2O_3 addition, (e) 5 mol % Ga_2O_3 addition and (f) 7 mol % Ga_2O_3 addition. Blank and solid symbols correspond to the impedance data before and after galvanostatic cycling test, respectively.

3.3. Tolerance for Li dendrite growth of Ta-doped LLZO with Ga_2O_3 addition

Next, we discuss the tolerance for Li dendrite growth in Ta-doped LLZO sintered with or without Ga_2O_3 addition. Nyquist plots for complex impedance $Z' + jZ''$ at room temperature for Li symmetric cells composed of each solid electrolyte samples are shown in Figure 6. Before the galvanostatic testing, the plot for each symmetric cell is composed of a large semicircle with a characteristic frequency from 2.5 to 4.5 MHz and a small distorted one at low frequency range from 100 Hz to 0.1 MHz. The contribution of ionic conduction for sintered Ta-LLZO with or without Ga_2O_3 addition was obtained from the high frequency (> 0.1 MHz) impedance data, and the diameters of semicircle at higher frequency rage well correlate with the difference in σ_{total} summarized in Table 1. The contribution of Interfacial charge transfer resistance R_{int} are contained at frequency range from 100 Hz to 0.1 MHz [16,49]. For the cells with 3 mol % and 5 mol % added Ta-doped LLZO, R_{int} seems to be larger than others but the value is estimated to be approximately 15 Ω cm². For other four symmetric cells, it is considered that the contribution of R_{int} is partly contained in a large semicircle [49] and its values are well below 10 Ω cm². The difference in R_{int} among the tested cells may be caused by the variations in the surface microstructures of the samples before attached Li metals.

Preprints (www.preprints.org) | NOT PEER-REVIEWED | Posted: 13 July 2022 doi:10.20944/preprints202207.0199.v1

Figure 7 shows the voltage response in galvanostatic cycling of each symmetric cell tested at room temperature. In this work, applied current density was firstly set to 0.05 mA cm^{-2}, and was increased 0.05 mA cm^{-2} around five cycles. As can be seen, voltage drops are increased gradually with increasing the current densities applied to the symmetric cell, but the sudden drops and fluctuation of cell voltages occur at specific current density, indicating that potential Li dendrites growth and propagation into a solid electrolyte at this point. After the cycling test of each cell discussed in later, we also confirmed the decrease in cell impedance shown in Figure 6. Several symmetric cells have higher residual impedance and the plots shaped like part of a semicircle, suggesting that these cells are not shorted completely [49].

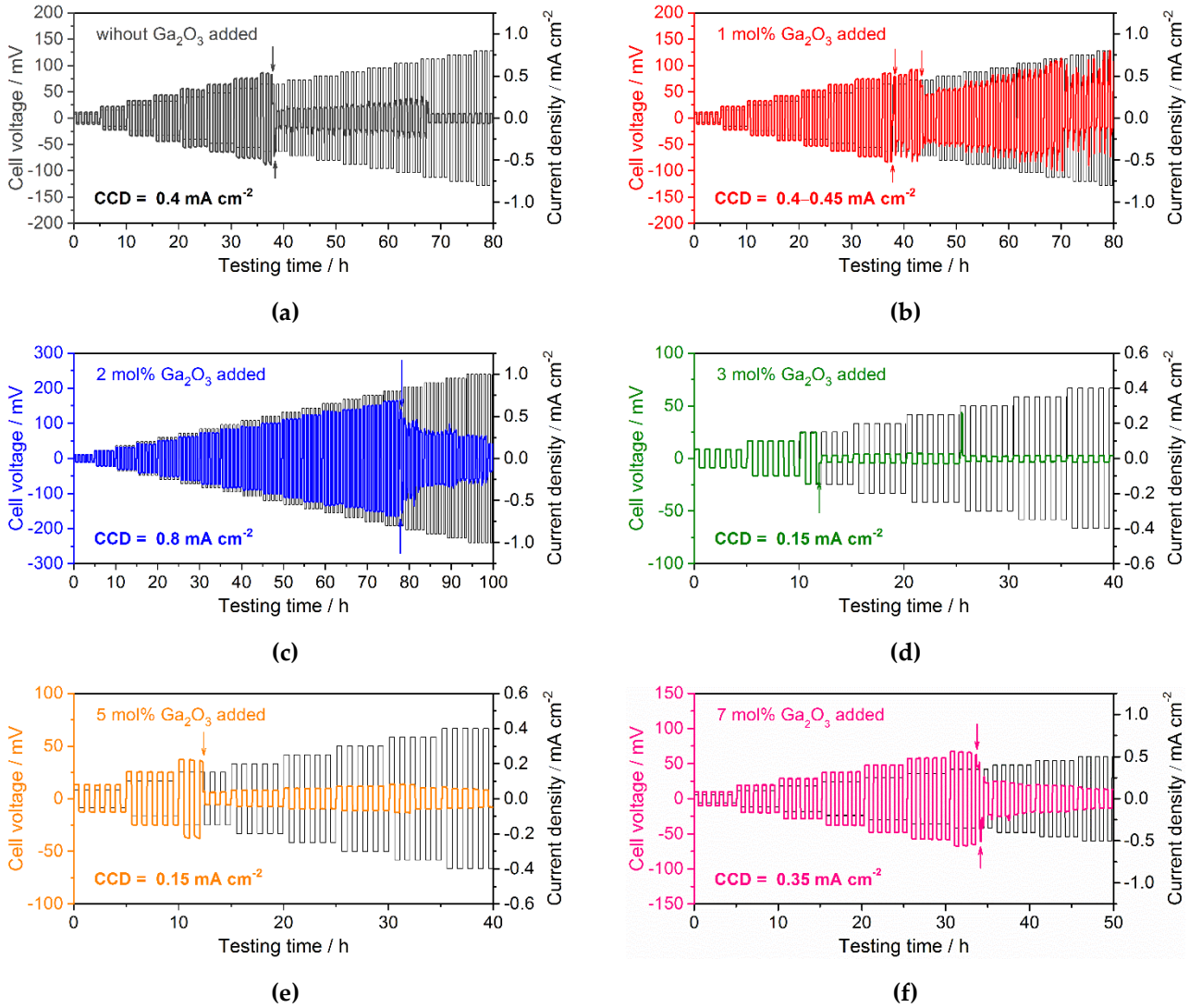

Figure 7. Cell voltage changes during galvanostatic cycling test at 25 ºC for Li symmetric cell with Ta-doped LLZO: (a) without Ga_2O_3 addition, (b) 1 mol % Ga_2O_3 addition, (c) 2 mol % Ga_2O_3 addition, (d) 3 mol % Ga_2O_3 addition, (e) 5 mol % Ga_2O_3 addition and (f) 7 mol % Ga_2O_3 addition. Vertical allows in each graph represents the sudden voltage drops caused by possible Li dendrite growth into a solid electrolyte.

The current density at which potential Li dendrite growth and propagation in a solid electrolyte occurred is commonly called as critical current density (CCD). CCD may be affected by the testing method because the interface condition between Li metal and a solid electrolyte is generally changed by the area-specific capacity and cycling numbers of Li plating/stripping cycling [7,18–20]. Therefore, when directly comparing the CCD

Preprints (www.preprints.org) | NOT PEER-REVIEWED | Posted: 13 July 2022 doi:10.20944/preprints202207.0199.v1

value with the data reported by other groups, it is necessary to pay attention to the difference in the test conditions. In this work, the method and condition for galvanostatic cycling test in this work are unified and the difference in R_{int} between the samples is adjusted to be as small as possible, so that CCD can be used for discussing the difference in the tolerance for Li dendrite growth depending on the microstructure of solid electrolyte. CCD for 1 mol % Ga_2O_3 added sample (Figure 7(b)) is confirmed to be 0.40–0.45 mA cm^{-2} and close to the sample without Ga_2O_3 addition (Figure 7(a)). 2 mol % Ga_2O_3 added shows the highest CCD of 0.8 mA cm^{-2} but 3 mol % or more Ga_2O_3 added samples show low CCD < 0.4 mA cm^{-2}. CCD of 3 and 5 mol % Ga_2O_3 added samples are the lowest (= 0.15 mA cm^{-2}) while 7 mol % Ga_2O_3 added sample shows higher CCD of 0.35 mA cm^{-2}. The difference in CCD values among 3–7 mol % Ga_2O_3 added samples composed of large-sized grains may be caused by the slight difference in R_{int} confirmed in Figure 6.

In Figure 8, σ_{total} and CCD are plotted against the amounts of Ga_2O_3 addition. The optimum amount of Ga_2O_3 added to Ta-doped LLZO for σ_{total} and CCD is completely different. It is worth noting that using 2 mol % Ga_2O_3 added sample, we also fabricated another Li symmetric cell with larger R_{int} (= 40 Ω cm^2) by changing the condition for cell stacking and galvanostatic cycling test was carried out under same condition. Although the polarization becomes larger by large R_{int}, the cell was cycled at current density above 0.5 mA cm^{-2} without any evidences of short circuit by Li dendrite growth and CCD attained to 0.6 mA cm^{-2} (Figure S2 in Supplementary Materials), which is better than symmetric cells with another solid electrolyte samples and lower R_{int} shown in Figure 7. This result support that in our current work, the optimum Ga_2O_3 amount added to Ta-doped LLZO is 2 mol % to obtain higher CCD. Excess Ga_2O_3 addition causes the degradation of Li dendrite tolerance of Ta-doped LLZO due to the abnormal grain growth promoted by liquid phase sintering.

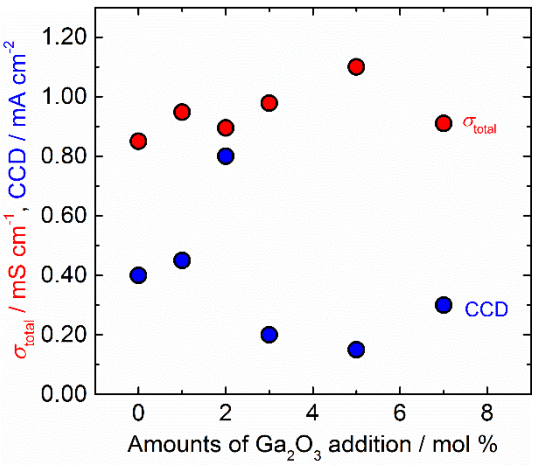

Figure 8. The total ionic conductivity σ_{total} and critical current density CCD at room temperature of all sintered samples plotted against the amounts of Ga_2O_3 addition.

Although our results reported here is the opposite of the result obtained in hot-pressed Al-doped LLZO followed by high temperature (1300 °C) and long-time annealing in Ar atmosphere [34], we believe dense structure with tightly connected small Ta-doped LLZO grains (below 10 μm) is suitable to obtain higher CCD, because uniform and dense structure composed of small-sized LLZO grains effectively enhance the fracture toughness of sintered samples [35–37]. We are now optimizing the sintering condition for Ga_2O_3 added Ta-doped LLZO carefully, to reduce the grain size and improve the structural uniformity further to enhance the tolerance for Li dendrite growth and the results will be presented in a forthcoming paper.

5. Conclusions

In conclusion, we synthesized Ga_2O_3 added Ta-doped LLZO with garnet-type structure using a conventional solid-state reaction method and examined their microstructures and electrochemical properties. When the amounts of Ga_2O_3 additive were below 2 mol %, the sintered sample has a dense structure mainly composed of grains with the averaged size of 5–10 μm, while 3 mol % or more Ga_2O_3 addition causes the significant increase in grain size above several 10 to 100 μm, due to the liquid phase sintering with certain amount of Li-Ga-O. The highest total ionic conductivity of 1.1 mS cm^{-1} at room temperature was obtained in 5 mol % Ga_2O_3 added sample, but in galvanostatic testing of the symmetric cell with Li metal electrodes, this sample was shorted by Li dendrite growth into solid electrolyte at current density below 0.2 mA cm^{-2}. The tolerance for Li dendrite growth is maximized in sample sintered with 2 mol % Ga_2O_3 addition, which was shorted at 0.8 mA cm^{-2} in the symmetric cell. Since the method and condition for galvanostatic cycling test are unified and the difference in Rint between the samples is adjusted to be as small as possible, the difference in CCD among the samples with different amounts of Ga_2O_3 addition are mainly governed by the difference in microstructures. Dense structure with tightly connected small Ta-doped LLZO grains is suitable to improve the tolerance for Li dendrite growth.

Supplementary Materials: The following are available online at www.mdpi.com/xxx/s1, Figure S1: Temperature dependence for total ionic conductivity σ_{total} for Ta-LLZO sintered with or without Ga_2O_3 addition, Figure S2: Nyquist plot for complex impedance and voltage response in galvanostatic cycling test for Li symmetric cell with larger interfacial resistance R_{int} composed with 2 mol % Ga_2O_3 added Ta-doped LLZO.

Author Contributions: Conceptualization, Y.Y. and R.I.; methodology, Y.Y, S.M. K.A. and R.I.; validation, Y.Y, S.M. K.A. and R.I.; formal analysis, Y.Y. and R.I.; investigation, Y.Y, S.M. K.A. and R.I.; resources, R.I.; data curation, Y.Y, S.M. K.A. and R.I.; writing—original draft preparation, Y.Y. and R.I.; writing—review and editing, R.I.; supervision, R.I.; project administration, R.I.; funding acquisition, R.I. All authors have read and agreed to the published version of the manuscript.

Funding: This work was partly supported by Grant-in-Aid for Scientific Research (JSPS KAKENHI) Grant Number 19H02128 and 22H01468 from the Japan Society for the promotion of Science (JSPS).

Acknowledgments: We acknowledged the support of the Cooperative Research Facility Center at Toyohashi University of Technology.

Conflicts of Interest: The authors declare no conflict of interest. The funders had no role in the design of the study; in the collection, analyses, or interpretation of data; in the writing of the manuscript, or in the decision to publish the results.

References

1. Zheng, F.; Kotobuki, M.; Song, S.; Lei, M.O.; Lu, L. Review on solid electrolytes for all-solid-state lithium-ion batteries. *J. Power Sources* **2018**, *389*, 198–213.
2. Takada, K. Progress in solid electrolytes toward realizing solid-state lithium batteries. *J. Power Sources* **2018**, *394*, 74–85.
3. Ren, Y.; Chen, K.; Chen, R.; Liu, T.; Zhang, Y.; Nan, C. Oxide electrolytes for lithium batteries. *J. Ame. Ceram. Soc.* **2015**, *98*, 3603–3623.
4. Murugan, R.; Thangadurai, V.; Weppner, W. Fast lithium ion conduction in garnet-type $Li_7La_3Zr_2O_{12}$. *Angew. Chem. Int. Ed.* **2007**, *46*, 7778–7781.
5. Samson, A.J.; Hofstetter, K.; Bag, S.; Thangadurai, V. A bird's-eye view of Li-stuffed garnet-type $Li_7La_3Zr_2O_{12}$ ceramic electrolytes for advanced all-solid-state Li batteries. *Energy Environ. Sci.* **2019**, *12*, 2957–2975.
6. Wang, C.; Fu, K.; Palakkathodi Kammampata, S.; McOwen, D.W.; Zhang, L.; Hitz, G.T.; Nolan, A.; Samson, A.; Wachsman, E.D.; Mo, Y.; Thangadurai, V.; Hu, L. Garnet-type solid-state electrolytes: materials, interfaces, and batteries. *Chem. Rev.* **2020**, *120*, 4257–4300.
7. Alexander, G.V.; Indu, M.S.; Murugan, R. Review on the critical issues for the realization of all-solid-state lithium metal batteries with garnet electrolyte: interfacial chemistry, dendrite growth, and critical current densities, Ionics **2021**, *27*, 4105–4126.

8. Patra, S.; Narayanasamy, J.; Panneerselvam, Murugan, R. Review—Microstructural modification in lithium garnet solid-state electrolytes: Emerging trends. *J. Electrochem. Soc.* **2022**, *169*, 030548.
9. Chen, B.; Sarkar, S.; Kammampata, S.P.; Zhou, C.; Thangadurai, V. Li-stuffed garnet electrolytes: structure, ionic conductivity, chemical stability, interface, and applications. *Canadian J. Chem.* **2022**, *100*, 311–319.
10. Kim, Y.; Yoo, A.; Schmidt, R.; Sharafi, A.; Lee, H.; Wolfenstine, J.; Sakamoto, J. Electrochemical Stability of $Li_{6.5}La_3Zr_{1.5}M_{0.5}O_{12}$ (M = Nb or Ta) against Metallic Lithium. *Front. Energy Res.* **2016**, *4*, 20.
11. Zhu, Y.; Connell, J.G.; Tepavcevic, S.; Zapol, P.; Garcia-Mendez, R.; Taylor, N.J.; Sakamoto, J.; Ingram, B.J.; Curtiss, L.A.; Freeland, J.W.; Fong D.D.; Markovic, N.M. Dopant-dependent stability of garnet solid electrolyte interfaces with lithium metal. *Adv. Energ. Mater.* **2019**, *9*, 1803440.
12. Tsai, C-L.; Tran, N.T.T.; Schierholz, R.; Liu, Z.; Windmüller, A.; Lin, C-A.; Zu, Q.; Lu, X.; Yu, S.; Tempel, H.; Kungl, H.; Lin, S-K.; Eichel, R-A. Instability of Ga-substituted $Li_7La_3Zr_2O_{12}$ toward metallic Li. *J. Mater. Chem. A* **2022**, *10*, 10998–11009.
13. McClelland, I; El-Shinawi, H.; Booth S.G.; Regoutz, A.; Clough, J.; Altus, S.; Cussen, E.J.; Baker, P.J.; Cussen, S.A. The role of the reducible dopant in solid electrolyte–lithium metal interfaces. *Chem. Mater.* **2022**, *34*, 5054–5064.
14. Ren, Y.; Shen, Y.; Lin, Y.; Nan, C.-W. Direct observation of lithium dendrites inside garnet-type lithium-ion solid electrolyte. *Electrochem. Commun*. **2015**, *57*, 27–30.
15. Cheng, E.J.; Sharafi, A.; Sakamoto, J. Intergranular Li metal propagation through polycrystalline $Li_{6.25}Al_{0.25}La_3Zr_2O_{12}$ ceramic electrolyte. *Electrochim. Acta* **2017**, *223*, 85–91.
16. Inada, R.; Yasuda, S.; Hosokawa, H. Saito, M.; Tojo, T.; Sakurai, Y. Formation and stability of interface between garnet-type Ta-doped $Li_7La_3Zr_2O_{12}$ solid electrolyte and lithium metal electrode. *Batteries* **2018**, *4*, 26.
17. Kazyak, E.; Garcia-Mendez, R.; LePage, W.S.; Sharafi, A.; Davis, A.L.; Sanchez, A.J.; Chen, K-H.; Haslam, C.; Sakamoto, J.; Dasgupta N.P. Li penetration in ceramic solid electrolytes: operando microscopy analysis of morphology, propagation, and reversibility. *Matter* **2020**, *2*, 1025–1048.
18. Sharafi, A.; Kazyak, E.; Davis, A.L.; Yu, S.; Thompson, T.; Siegel, D.J.; Dasgupta, N.P.; Sakamoto, J. Surface chemistry mechanism of ultra-low interfacial resistance in the solid-state electrolyte $Li_7La_3Zr_2O_{12}$. *Chem. Mater.* **2017**, *29*, 7961–7968.
19. Basappa, R.H.; Ito, T.; Yamada, H. Contact between garnet-type solid electrolyte and lithium metal anode: Influence on charge transfer resistance and short circuit prevention. *J. Electrochem. Soc.* **2017**, *164*, A666–A671.
20. Taylor, N.J.; Stangeland-Molo, S.; Haslam, C.G.; Sharafi, A.; Thompson, T.; Wang, M. Garcia-Mendez, R.; Sakamoto, J. Demonstration of high current densities and extended cycling in the garnet $Li_7La_3Zr_2O_{12}$ solid electrolyte. *J. Power Sources* 2018, **396**, 314–318.
21. Motoyama, M.; Tanaka, Y.: Yamamoto, T.; Tsuchimine, N.; Kobayashi S.; Iriyama, Y. The Active interface of Ta-doped $Li_7La_3Zr_2O_{12}$ for Li plating/stripping revealed by acid aqueous etching. *ACS Appl. Energ. Mater.* **2019**, *2*, 6720−6731.
22. Tsai, C.-L.; Roddatis, V.; Chandran, C.V.; Ma, Q.; Uhlenbruck, S.; Bram, M.; Heitjans, P.; Guillon, O. $Li_7La_3Zr_2O_{12}$ interface modification for Li dendrite prevention. *ACS Appl. Mater. Interfaces* **2016**, *8*, 10617–10626.
23. Han, X.; Gong, Y.; Fu, K.; He, X.; Hitz, G.T.; Dai, J.; Pearse, A.; Liu, B.; Wang, H.; Rublo, G.; Mo, Y.; Thangadurai, V.; Wachsman E.D.; Hu, L. Negating interfacial impedance in garnet-based solid-state Li metal batteries. *Nat. Mater.* **2017**, *16*, 572–579.
24. Huang, X.; Lu, Y.; Guo, H.; Song, Z.; Xiu, T.; Badding, M.E.; Wen, Z. None-mother-powder method to prepare dense Li-garnet solid electrolytes with high critical current density. *ACS Appl. Energy Mater.* **2018**, 1, 5355–5365.
25. Zhou, C.; Samson, A.J.; Hofstetter K.; Thangadurai V. A surfactant-assisted strategy to tailor Li-ion charge transfer interfacial resistance for scalable all-solid-state Li batteries. *Sust. Energy Fuels* **2018**, *2*, 2165–2170.
26. Sastre, J.; Futscher, M.H.; Pompizi, L.; Aribia, A.; Priebe, A.; Overbeck, J.; Stiefel, M.; Tiwari, A.N.; Romanyuk, Y.E. Blocking lithium dendrite growth in solid-state batteries with an ultrathin amorphous Li-La-Zr-O solid electrolyte. *Commun. Mater.* **2021**, *2*, 76.
27. Du, M.; Sun, Y.; Liu, B.; Chen, B.; Liao, K.; Ran, R.; Cai, R.; Zhou, W.; Shao, Z. Smart construction of an intimate lithium | garnet interface for all-solid-state batteries by tuning the tension of molten lithium. *Adv. Funct. Mater.* **2021**, *31*, 2101556.
28. Guo, S.; Wu, T-T.; Sun, G.; Zhang, S-D.; Li, B.; Zhang, H-S.; Qi, M-Y.; Liu, X-H.; Cao, A-M.; Wan, L-J. Interface engineering of a ceramic electrolyte by Ta_2O_5 nanofilms for ultrastable lithium metal batteries. *Adv. Funct. Mater.* **2022**, *32*, 2201498.
29. Cheng, L.; Chen, W.; Kunz, M.; Persson, K.; Tamura, N.; Chen, G.; Doeff, M. Effect of surface microstructure on electrochemical performance of garnet solid electrolytes. *ACS Appl. Mater. Interfaces* **2015**, *7*, 2073–2081.

30. Sharafi, A.; Meyer, H.M.; Nanda, J.; Wolfenstine, J.; Sakamoto, J. Controlling and correlating the effect of grain size with the mechanical and electrochemical properties of $Li_7La_3Zr_2O_{12}$ solid-state electrolyte. *J. Mater. Chem. A* **2017**, *5*, 21491–21504.
31. Matsuki, Y.; Noi, K.; Deguchi, M.; Sakuda, A.; Hayashi, A.; Tatsumisago, M. Lithium dissolution/deposition behavior of Al-doped $Li_7La_3Zr_2O_{12}$ ceramics with different grain sizes. J. Electrochem. Soc. **2019**, *166*, A5470
32. Basappa, R.H.; Ito, T.; Morimura, T.; Bekarevich, R.; Mitsuishi, K.; Yamada, H. Grain boundary modification to suppress lithium penetration through garnet-type solid electrolyte. *J. Power Sources* **2017**, *363*, 145–152.
33. Xu, B.; Li,W.; Duan, H.; Wang, H.; Guo, Y.; Li, H.; Liu, H. Li_3PO_4-added garnet-type $Li_{6.5}La_3Zr_{1.5}Ta_{0.5}O_{12}$ for Li-dendrite suppression. *J. Power Sources* **2017**, *354*, 68–73.
34. Hosokawa, H.; Takeda, A.; Inada, R.; Sakurai, Y. Tolerance for Li dendrite penetration in Ta-doped $Li_7La_3Zr_2O_{12}$ solid electrolytes sintered with $Li_{2.3}C_{0.7}B_{0.3}O_3$ additive. *Mater. Lett.* **2020**, *279*, 128481.
35. Hong, M.; Dong, Q.; Xie, H.; Clifford, B.C.; Qian, J.; Wang, X.; Luo, J.; Hu, L. Ultrafast sintering of solid-state electrolytes with volatile fillers. *ACS Energy Lett.* **2021**, *6*, 3753–3760.
36. Guo, H.; Su, J.; Zha, W.; Xiu, T.; Song, Z.; Badding M.E.; Jin, J.; Wen, Z. Achieving high critical current density in Ta-doped $Li_7La_3Zr_2O_{12}$/MgO composite electrolytes, *J. Alloys Compd.* **2021**, *856*, 157222.
37. Zheng, C.; Ruan, Y.; Su, J.; Song, Z.; Xiu, T.; Jin, J. Badding M.E.; Wen, Z. Grain boundary modification in garnet electrolyte to suppress lithium dendrite growth, *Chem. Eng. J.* **2021**, *411*, 128508.
38. Hitz, G.T.; McOwen, D.M.; Zhang, L.; Ma, Z.; Fu, Z.; Wen, Y.; Gong, Y.; Dai, J.; Hamann, T.R.; Hu, L.; Wachsman, E.D. High-rate lithium cycling in a scalable trilayer Li-garnet-electrolyte architecture. *Mater. Today* **2019**, *22*, 50–57.
39. Huo, H.; Liang, J.; Zhao,N.; Li, X.; Lin, X.; Zhao, Y.; Adair, K.; Li, R.; Guo, X.; Sun, X. Dynamics of the garnet/Li interface for dendrite-free solid-state batteries. *ACS Energy Lett.* **2020**, *5*, 2156−2164.
40. Koshikawa, H.; Matsuda, S.; Kamiya, K.; Miyayama, M.; Kubo, Y.; Uosaki, K.; Hashimoto K. Nakanishi, S. Electrochemical impedance analysis of the Li/Au-$Li_7La_3Zr_2O_{12}$ interface during Li dissolution/deposition cycles: Effect of pre-coating $Li_7La_3Zr_2O_{12}$ with Au. *J. Electroanal. Chem.* **2019**, *835*, 143–149.
41. Wang, M.; Wolfenstine J.; Sakamoto, J. Temperature dependent flux balance of the Li/$Li_7La_3Zr_2O_{12}$ interface. *Electrochim. Acta* **2019**, *296*, 842–847.
42. Wang, M.; Choudhury, R.; Sakamoto, J. Characterizing the Li-solid-electrolyte interface dynamics as a function of stack pressure and current density. *Joule* **2019**, *3*, 2165–2178.
43. Krauskopf, T.; Mogwitz, B. Hartmann, H. Singh, D.K.; Zeier, W.G.; Janek, J. The fast charge transfer kinetics of the lithium metal anode on the garnet-type solid electrolyte $Li_{6.25}Al_{0.25}La_3Zr_2O_{12}$. *Adv. Energy Mater.* **2020**, *10*, 2000945.
44. Liu, X.; Garcia-Mendez, R.; Lupini, A.R.; Cheng, Y.; Hood, Z.D.; Han, F.; Sharafi, A.; Idrobo, J.C.; Dudney, N.J.; Wang, C.; Ma, C.; Sakamoto, J.; Chi, M. Local electronic structure variation resulting in Li 'filament' formation within solid electrolytes, *Nat. Mater.* **2021**, ***20***, 1485–1490.
45. Cao, D.; Sun, X.; Li, Q.; Natan, A.; Xiang, P.; Zhu, H. Lithium dendrite in all-solid-state batteries: growth mechanisms, suppression strategies, and characterizations. *Matter* **2020**, *3*, 57–94.
46. Lu, Y.; Zhao, C-Z.; Yuan, H.; Cheng, X-B.; Huang, J-Q.; Zhang, Q. Critical current density in solid-state lithium metal batteries: mechanism, influences, and strategies. *Adv. Funct. Mater.* **2021**, *31*, 2009925.
47. Sarkar, S.; Thangadurai, V. Critical current densities for high-performance all-solid-state Li-metal batteries: Fundamentals, mechanisms, interfaces, materials, and applications. *ACS Energy Lett.* **2022**, *7*, 1492–1527.
48. Matsuda, Y.; Sakaida, A.; Sugimoto, K.; Mori, D.; Takeda, Y.; Yamamoto, O.; Imanishi, N. Sintering behavior and electrochemical properties of garnet-like lithium conductor $Li_{6.25}M_{0.25}La_3Zr_2O_{12}$ (M: Al^{3+} and Ga^{3+}). *Solid State Ion.* **2017**, 311, 69–74.
49. Inada, R.; Takeda, A.; Yamazaki, Y.; Miyake, S.; Sakurai, Y.; Thangadurai, V.; Effect of postannealing on the properties of a Ta-doped $Li_7La_3Zr_2O_{12}$ solid electrolyte degraded by Li dendrite penetration. *ACS Appl. Energy Mater.* **2020**, *3*, 12517–12524.
50. Awaka, J.; Takashima, A.; Kataoka, K.; Kijima, N.; Idemoto, Y.; Akimoto, J. Crystal structure of fast lithium-ion-conducting cubic $Li_7La_3Zr_2O_{12}$. *Chem. Lett.* **2011**, *40*, 60–62.